

# Mechanical dissipation in MoRe superconducting metal drums

S. Yanai, V. Singh, M. Yuan, M. Gely, S. J., Bosman, and G. A., Steele

*Department of Quantum Nanoscience,*

*Kavli Institute of Nanoscience, Delft University of Technology,*

*Lorentzweg 1, 2628 CJ Delft, The Netherlands.*

(Dated: October 9, 2018)

## Abstract

We experimentally investigate dissipation in mechanical resonators made of a disordered superconducting thin film of Molybdenum-Rhenium(MoRe) alloy. By electrostatically driving the drum with a resonant AC voltage, we detect its motion using a superconducting microwave cavity. From the temperature dependence of mechanical resonance frequencies and quality factors, we find evidence for non-resonant, mechanically active two-level systems (TLSs) limiting its quality factor at low temperature. In addition, we observe a strong suppression of mechanical dissipation at large mechanical driving amplitudes, suggesting an unconventional saturation of the non-resonant TLSs. These new observations shed light on the mechanism of mechanical damping in superconducting drums and routes towards understanding dissipation in such mechanical systems.

Nanoelectromechanical systems have evolved into an important platform in modern information technology. They are extensively used for applications in sensing, filtering and timing<sup>1</sup>. One remarkable example is cavity opto/electro-mechanics<sup>2,3</sup>. The demonstrations of the quantum ground state of mechanical resonators have opened new applications of NEMS devices in quantum information technology<sup>4,5</sup>. To this end, the approach of cavity optomechanics which uses the interaction between light and mechanical motion, has been very successful and enabled the applications of NEMS towards the near-quantum limited frequency conversion<sup>6,7</sup>, temporal and spectrum shaping of signals<sup>8</sup>, and a nearly quantum limited frequency-mixer<sup>9</sup>.

A successful implementation of an optomechanical system is realized by coupling a superconducting drumhead resonator to a microwave cavity. For quantum-limited performance of such a coupled system, both the drumhead resonator and the superconducting cavity should have low dissipation rates. In recent years, superconducting metal drums<sup>10</sup> have emerged as a popular platform for microwave optomechanics. While such drums can exhibit very low dissipation, there is also a large spread in reported mechanical Q-factors<sup>10-13</sup> and not many reports studying the dissipation mechanisms in such devices.

Here, we explore mechanical dissipation mechanisms in such superconducting drum resonators as a function of temperature and driving amplitude. The variation of dissipation rate and resonant frequency with temperature suggest that mechanically active two-level systems (TLSs)<sup>14,15</sup> play an important role, setting the dissipation in these disordered superconductors akin to acoustic studies performed earlier on superconducting glasses<sup>16</sup>. By varying the acoustic excitation strength, we further observe an amplitude dependent damping rate supporting the role of TLSs, similar to the observations made in superconducting microwave resonators in response to the electromagnetic field<sup>17,18</sup> with electrical TLSs, but with an unconventional saturation of the non-resonant mechanical TLSs by the mechanical drive.

The drums studied in this letter were made using films of a superconducting alloy of Molybdenum and Rhenium (MoRe 60-40). The compatibility of MoRe with HF, oxygen plasma, and an elastic modulus of  $\approx 1$  GPa makes it an attractive candidate for making hybrid electromechanical devices<sup>19</sup>. The electrical properties of MoRe are well studied establishing its disordered nature with a residual resistance ratio of approximately unity and a superconducting transition temperature of 9.2 K<sup>20-23</sup>. The electrical dissipation of such

films in microwave frequency domain has been characterized in earlier studies<sup>24</sup>, as well as recent reports in coplanar waveguides<sup>25</sup>.

Fig. 1(a) shows an optical microscope image of our complete optomechanical device. It consists of a superconducting drumhead resonator and a high-impedance microwave cavity both made of MoRe. The mechanically compliant drumhead resonator is galvanically shorted to the high-impedance microwave cavity, enabling electrostatic actuation of its motion. The microwave cavity is coupled through the drumhead to the feedline, such that its response can be accessed in a reflection measurement. Fig. 1(b) shows a scanning electron microscope image of the drumhead resonator. We apply microwave signals to the cavity via a mechanically compliant capacitor. Detection of the motion of the drum occurs through its modulation of the cavity frequency,  $\omega_c$ , as well as the external cavity decay rate,  $\kappa_e$  as schematically shown in Fig. 1(c).

To actuate the drumhead resonator, we apply a DC signal  $V_{dc}$  and a small RF signal  $V_{ac}$  near the mechanical resonance frequency  $\omega_m$  simultaneously to the input port. Due to capacitive attraction, this signal exerts a force  $C'_g V_{dc} V_{ac}$  on the drumhead resonator, where  $C'_g = dC_g/dx$  is the derivative of the capacitance between the resonator and the feedline with respect to distance. In order to read out the mechanical motion, we drive the system with a microwave tone at the cavity resonance frequency  $\omega_c$ . Due to electro-mechanical coupling, mechanical motion modulates the intra-cavity power, creating sideband signals in the reflected signal. The sideband signals are amplified and then mixed down with a local oscillator tone at the cavity resonance frequency. The signal is further amplified and sent to a spectrum analyzer. Using the mechanical resonator as the coupling capacitor to the cavity enables both direct electrostatic actuation of the motion and tuning of the mechanical resonance frequency using voltages applied to the feedline.

The fabricated samples are placed in a radiation-tight box and cooled down to 20 mK in a dilution refrigerator with sufficient attenuation at each temperature stage to thermalize the microwave signals (see Supplementary Materials for measurement chain schematic (SM)). We first begin by characterizing the microwave cavity. The microwave cavity has a resonance frequency of  $\omega_c = 2\pi \times 6.30$  GHz, external coupling rate  $\kappa_e = 2\pi \times 31.0$  MHz, and internal dissipation rate of  $\kappa_i = 2\pi \times 25.8$  MHz (see SM for detailed measurements). The red curve in Fig. 2(a) shows the measured mechanical response of the resonator along with a skewed-Lorentzian fit (light-blue line). The slight asymmetry in the measured homodyne

signal arises from the finite electrical isolation and is discussed in the supplementary material. From the fit, we find a mechanical resonance frequency of  $\omega_m = 7.2885$  MHz with a quality-factor  $Q_m$  of  $50 \times 10^3$  at  $V_{dc} = 10$  V. Fig. 2(b) shows a colorscale plot of mechanical response as a function of frequency of the RF signal and DC voltage applied to the feedline using a bias tee. The sharp change in color reflects the mechanical resonance frequency. As the DC voltage is tuned away from zero, the mechanical resonance frequency decreases quadratically, showing the well-studied capacitive softening effect<sup>26</sup>. The mechanical frequency is pulled by 200 kHz for gate voltages of 20 V. The mechanical signal is no longer visible around zero gate voltage due to the vanishing electrostatic force.

In Fig. 3, we investigate the temperature dependence of the mechanical response from 23 mK to 1.5 K. We measured the mechanical resonance frequencies and the quality-factors at different temperatures and at different applied dc voltages,  $V_g = 7, 14,$  and 28 V. Fig 3(a) shows the normalized shift in the resonance frequency for various temperature points. As the temperature is increased the resonance frequency increases logarithmically up to a cross-over temperature of  $\approx 900$  mK. At higher temperatures, we see a slight drop in the resonance frequency. Fig. 3(b) shows the quality-factor  $Q_m$  change as a function of temperature. As the temperature is increased from 23 mK,  $Q_m$  shows a sharp decrease for all gate voltages. Above the approximate cross-over temperature observed in the mechanical frequency,  $Q_m$  stops decreasing and saturates at a value around 10,000.

The logarithmic increase in the frequency shift suggests the presence of two-level systems<sup>16,27-29</sup>. TLSs can have a very broad spectral distribution<sup>30</sup>. At temperatures  $k_B T \gg \hbar\omega_m$ , the resonant TLSs are expected to be saturated, and not able to contribute to mechanical dissipation. However, coupling of the mechanical motion to higher energy, off-resonant TLSs can still have a significant contribution to the frequency shift. Comparing results at three different voltages, the normalized shifts are independent of mechanical resonant frequency below the cross over temperature. Such a temperature dependence can also be interpreted in the context of a TLSs model: at high temperatures, part of the mechanical restoring force arises from the dispersive shift of the thermal population of the high frequency TLSs. Beyond the cross-over temperature, these TLSs decouple from the mechanics due to either changes of their thermal populations or the relaxation rate. As the TLSs are decoupled the mechanical spring constant reduces, giving a lower mechanical frequency. For an off-resonant dispersive interaction, the normalized frequency shift is expected to scale as

$\delta f/f_0 = C_s \log(T/T_0)$ , where  $C_s$  is a constant proportional to the filling factor and TLSs loss tangent<sup>30</sup>. For data shown in Fig 3(a), we find  $C_s \approx 4 \times 10^4$ , similar to previously reported values for mechanical TLSs in disordered superconducting films<sup>16,31</sup>.

To compare the behavior of dissipation with the frequency shift, we plot  $Q_m^{-1}$  in the subpanel of Fig. 3(b). In lower temperature ranges, we observe an increase in the mechanical dissipation rate with temperature, which slows down as the temperature approaches  $\approx 700$  mK. As discussed above, the interaction with resonant TLSs can be neglected due to the low frequency of the drum ( $k_B T \gg \hbar \omega_m$ ). Non-resonant TLSs, however, can also result in dissipation due to the lag between the dispersive shift of their energies due to the mechanical coupling and their equilibration time with the bath. The contribution of the off-resonant interaction to the damping scale as  $Q_m^{-1} = C_s \frac{\Gamma(T)}{\omega_m}$  for  $\omega_m > \Gamma(T)$ , where  $\Gamma$  is the TLSs relaxation rate<sup>30</sup>. The behavior observed here of mechanical dissipation suggest that TLSs relaxation rate increases linearly with the temperature.

In Fig. 4, we explore saturation effects of the TLSs in these drums by applying a large mechanical driving force. To increase the acoustic excitation strength, we varied the  $AC$  driving voltage for mechanical actuation. Fig. 4(a) shows mechanical responsivity (amplitude/ driving force) at different driving voltages in the linear and non-linear limits. Within the linear limit we see an increase in the responsivity as the drive signal is increased, suggesting an increase in the mechanical quality factor  $Q_m$ . The extracted quality factor is shown in Fig. 4(b). In the nonlinear limit (orange trace), we can also qualitatively deduce increase in  $Q_m$  from the increase in amplitude of the responsivity. Similar negative nonlinear damping characteristics were also observed in a similar second device.

While a decrease in the mechanical damping shown in figure 4 is similar to the case of the saturation of resonant TLSs in superconducting microwave cavities, such saturation effects are not typically observed when the interaction with the TLSs is non-resonant, as the non-resonant drive is not able to excite the TLSs directly. The observation presented here of decreased damping at large mechanical excitation, also recently reported for the case of graphene resonators<sup>32</sup>, suggests that a strongly non-equilibrium population of high frequency TLSs is induced by the low frequency driving forces, for example, by either strong higher-order excitation processes, or by a decoupling of the non-resonant TLSs from their bath.

In conclusion, we have studied dissipation in the mechanical drumhead resonators made of

superconducting alloy of MoRe. The temperature dependence of the dissipation and resonant frequency strongly suggest the presence of mechanically active TLSs in these disordered superconducting thin film mechanical resonators. At low temperatures the main contribution to dissipation and frequency shift stems from the dispersive interaction with TLSs, with slow relaxation rates  $< 7$  MHz. We further explored at the mechanical dissipation while varying the strength of acoustic field and observe an amplitude dependent damping, suggesting a non-equilibrium population of non-resonant TLSs induced by mechanical drive.

**Supplementary material** See supplementary material for device fabrication steps, cavity characterization, measurement setup and estimation of the mechanical amplitude.

**Acknowledgments** The work was supported by the Dutch Science Foundation (NWO/FOM).

- 
- <sup>1</sup> Ekinici, K. L. and Roukes, M. L. *Review of Scientific Instruments* **76**(6), 061101 June (2005).
  - <sup>2</sup> Aspelmeyer, M., Kippenberg, T. J., and Marquardt, F. *Reviews of Modern Physics* **86**(4), 1391–1452 December (2014).
  - <sup>3</sup> Metcalfe, M. *Applied Physics Reviews* **1**(3), 031105 September (2014).
  - <sup>4</sup> Teufel, J. D., Donner, T., Li, D., Harlow, J. W., Allman, M. S., Cicak, K., Sirois, A. J., Whittaker, J. D., Lehnert, K. W., and Simmonds, R. W. *Nature* **475**(7356), 359–363 July (2011).
  - <sup>5</sup> Chan, J., Alegre, T. P. M., Safavi-Naeini, A. H., Hill, J. T., Krause, A., Grblacher, S., Aspelmeyer, M., and Painter, O. *Nature* **478**(7367), 89–92 October (2011).
  - <sup>6</sup> Andrews, R. W., Peterson, R. W., Purdy, T. P., Cicak, K., Simmonds, R. W., Regal, C. A., and Lehnert, K. W. *Nature Physics* **10**(4), 321–326 April (2014).
  - <sup>7</sup> Bochmann, J., Vainsencher, A., Awschalom, D. D., and Cleland, A. N. *Nature Physics* **9**(11), 712–716 November (2013).
  - <sup>8</sup> Andrews, R. W., Reed, A. P., Cicak, K., Teufel, J. D., and Lehnert, K. W. *Nature Communications* **6**, 10021 November (2015).
  - <sup>9</sup> Lecocq, F., Clark, J. B., Simmonds, R. W., Aumentado, J., and Teufel, J. D. *arXiv:1512.00078 [quant-ph]* November (2015). arXiv: 1512.00078.
  - <sup>10</sup> Teufel, J. D., Li, D., Allman, M. S., Cicak, K., Sirois, A. J., Whittaker, J. D., and Simmonds,

- R. W. *Nature* **471**(7337), 204–208 March (2011).
- <sup>11</sup> Suh, J., Shaw, M. D., LeDuc, H. G., Weinstein, A. J., and Schwab, K. C. *Nano Letters* **12**(12), 6260–6265 December (2012).
- <sup>12</sup> Wollman, E. E., Lei, C. U., Weinstein, A. J., Suh, J., Kronwald, A., Marquardt, F., Clerk, A. A., and Schwab, K. C. *Science* **349**(6251), 952–955 August (2015).
- <sup>13</sup> Pirkkalainen, J.-M., Damskagg, E., Brandt, M., Massel, F., and Sillanpaa, M. *Physical Review Letters* **115**(24), 243601 December (2015).
- <sup>14</sup> Anderson, P. w., Halperin, B. I., and Varma, c. M. *Philosophical Magazine* **25**(1), 1–9 January (1972).
- <sup>15</sup> Phillips, W. A. *Reports on Progress in Physics* **50**(12), 1657 December (1987).
- <sup>16</sup> Raychaudhuri, A. K. and Hunklinger, S. *Zeitschrift fr Physik B Condensed Matter* **57**(2), 113–125 October (1984).
- <sup>17</sup> Gao, J., Daal, M., Vayonakis, A., Kumar, S., Zmuidzinias, J., Sadoulet, B., Mazin, B. A., Day, P. K., and Leduc, H. G. *Applied Physics Letters* **92**(15), 152505 April (2008).
- <sup>18</sup> Pappas, D. P., Vissers, M. R., Wisbey, D. S., Kline, J. S., and Gao, J. *IEEE Transactions on Applied Superconductivity* **21**(3), 871–874 June (2011).
- <sup>19</sup> Leonhardt, T., Carln, J.-C., Buck, M., Brinkman, C. R., Ren, W., and Stevens, C. O. In *AIP Conference Proceedings*, volume 458, 685–690. AIP Publishing, January (1999).
- <sup>20</sup> Lerner, E., Daunt, J. G., and Maxwell, E. *Physical Review* **153**(2), 487–492 January (1967).
- <sup>21</sup> Seleznev, V. A., Tarkhov, M. A., Voronov, B. M., Milostnaya, I. I., Lyakhno, V. Y., Garbuz, A. S., Mikhailov, M. Y., Zhigalina, O. M., and Goltsman, G. N. *Superconductor Science and Technology* **21**(11), 115006 November (2008).
- <sup>22</sup> Sundar, S., Sharath Chandra, L. S., Sharma, V. K., Chattopadhyay, M. K., and Roy, S. B. *AIP Conference Proceedings* **1512**(1), 1092–1093 February (2013).
- <sup>23</sup> Aziz, M., Hudson, D. C., and Russo, S. *Applied Physics Letters* **104**(23), 233102 June (2014).
- <sup>24</sup> Yasaitis, J. and Rose, R. *IEEE Transactions on Magnetics* **11**(2), 434–436 March (1975).
- <sup>25</sup> Singh, V., Schneider, B. H., Bosman, S. J., Merckx, E. P. J., and Steele, G. A. *Applied Physics Letters* **105**(22), 222601 December (2014).
- <sup>26</sup> Kozinsky, I., Postma, H. W. C., Bargatin, I., and Roukes, M. L. *Applied Physics Letters* **88**(25), 253101 June (2006).
- <sup>27</sup> Hoehne, F., Pashkin, Y. A., Astafiev, O., Faoro, L., Ioffe, L. B., Nakamura, Y., and Tsai, J. S.

*Physical Review B* **81**(18), 184112 May (2010).

- <sup>28</sup> Venkatesan, A., Lulla, K. J., Patton, M. J., Armour, A. D., Mellor, C. J., and Owers-Bradley, J. R. *Physical Review B* **81**(7), 073410 February (2010).
- <sup>29</sup> Imboden, M. and Mohanty, P. *Physics Reports* **534**(3), 89–146 January (2014).
- <sup>30</sup> Esquinazi, P., editor. *Tunneling Systems in Amorphous and Crystalline Solids*. Springer Berlin Heidelberg, Berlin, Heidelberg, (1998).
- <sup>31</sup> Esquinazi, P., Ritter, H. M., Neckel, H., Weiss, G., and Hunklinger, S. *Zeitschrift für Physik B Condensed Matter* **64**(1), 81–93 March (1986).
- <sup>32</sup> Singh, V., Shevchuk, O., Blanter, Y. M., and Steele, G. A. *arXiv:1508.04298 [cond-mat]* August (2015). arXiv: 1508.04298.



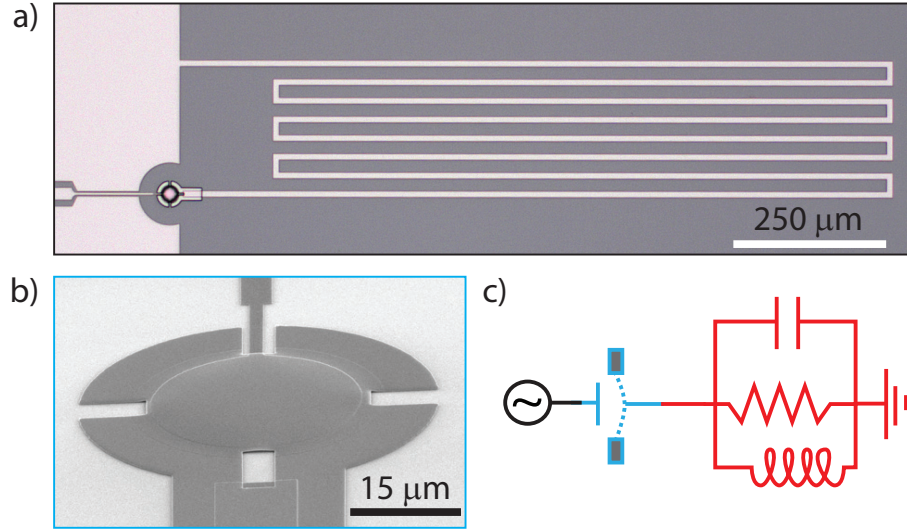


FIG. 1: Microwave cavity readout of a superconducting drum with electrostatic driving. a) Optical microscope image of the device. A drumhead mechanical oscillator is capacitively coupled to the microwave input port of a high impedance microwave cavity on a sapphire substrate. b) Scanning electron microscope image of MoRe drumhead resonator. The drum is  $30 \mu\text{m}$  in diameter and is suspended approximately  $290 \text{ nm}$  above the gate bottom electrode. c) Device schematic diagram: the mechanical drum is capacitively coupled to the microwave input port. Motion of the drum modulates both the resonance frequency  $\omega_c$  and the external coupling rate  $\kappa_e$  of the cavity.

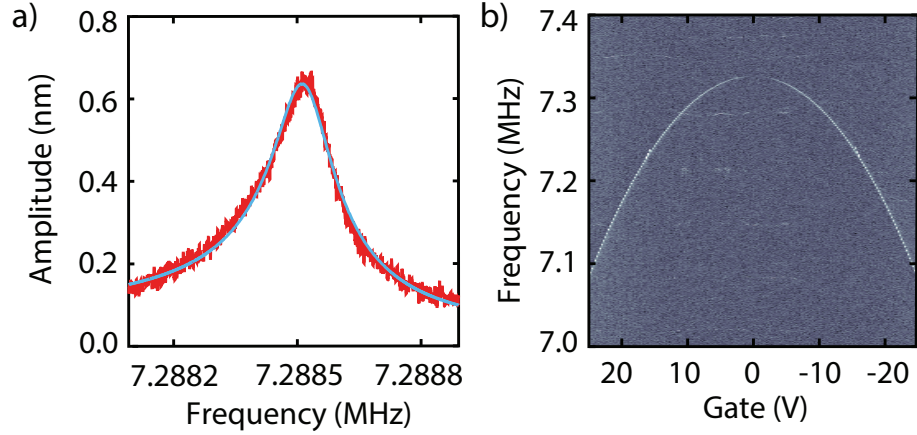


FIG. 2: Characterization of the mechanical response of the drumhead resonator. a) Mechanical response of MoRe drumhead resonator at 10 V of applied voltage (red curve) along with the fitted curve (light blue), yielding a quality-factor of 50248 and resonant frequency of 7.2885 MHz. b) Colorscale plot of the measured response with drive frequency and applied voltage. Mechanical response can be tuned over 200 kHz with  $\pm 28$  V of applied voltage.

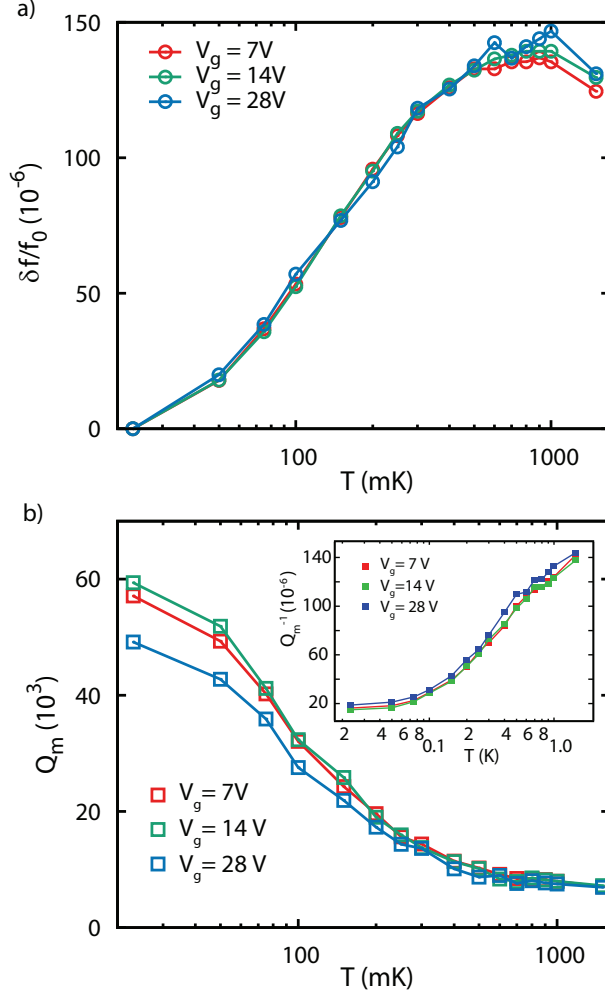


FIG. 3: Temperature dependence of a) Normalized relative frequency shift  $\delta f = (f_0(T) - f_0(23\text{ mK}))/f_0(23\text{ mK})$  and b) the mechanical quality factor. The mechanical quality-factor is determined from fitting to a Lorentzian function. Measurements are taken at three different voltages 7, 14, 28 V. The inset shows the plot of inverse quality-factor  $Q_m^{-1}$ .

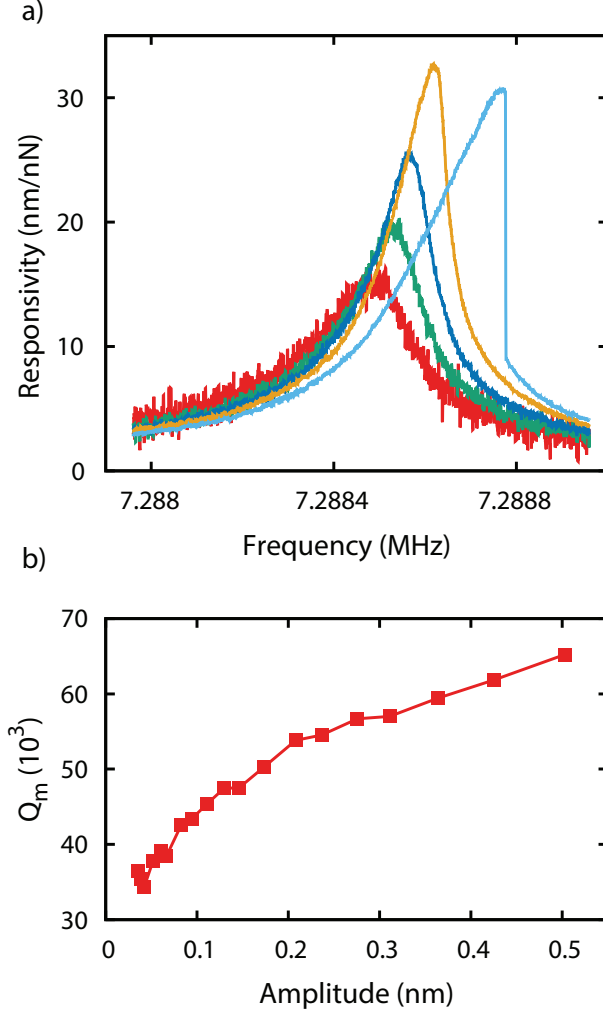


FIG. 4: Negative nonlinear damping of a superconducting metal drum. Mechanical responsivity ( $x_0/F_0$ ) of the drum for different driving forces (Red - light blue: 2.9, 5.8, 11.2, 29.3, 82.8 pN). As the driving force is increased (red-dark blue), the responsivity of the drum on resonance increases, indicating a increase in the mechanical quality-factor. As the drum is driven into the nonlinear regime (yellow), the  $Q_m$  continues to increase, and at higher powers, the  $Q_m$  in the nonlinear regime begins to drop, as can be seen by the decreased responsivity of the light blue curve. In the linear regime,  $Q_m$  is extracted by fitting the curves with a Lorentzian curve with a Fano correction. b) Mechanical quality-factor as a function of mechanical amplitudes. Actuation force is varied with different RF power on a signal generator for driving mechanics.

# Supplementary Material : Mechanical dissipation in MoRe superconducting metal drums

S. Yanai, V. Singh, M. Yuan, M. Gely, S. J., Bosman, and G. A., Steele

*Department of Quantum Nanoscience,*

*Kavli Institute of Nanoscience, Delft University of Technology,*

*Lorentzweg 1, 2628 CJ Delft, The Netherlands. and*

*Kavli Institute of NanoScience, Delft University of Technology,*

*PO Box 5046, 2600 GA, Delft, The Netherlands.*

(Dated: October 9, 2018)

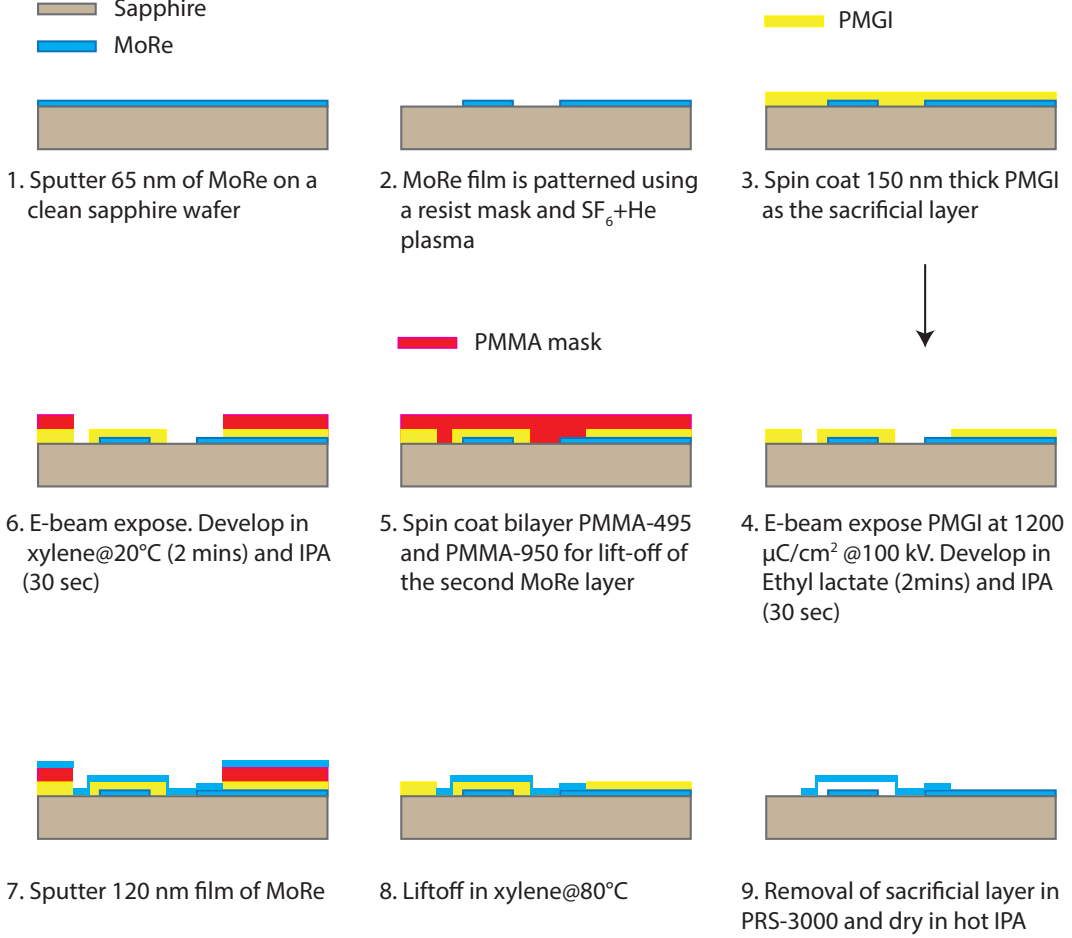


FIG. 1: An illustration of complete fabrication process with brief outline.

## I. FABRICATION DETAILS

The fabrication process is mainly based on using PMGI as the sacrificial layer together with its compatibility with PMMA based resist. Steps of the fabrication process are illustrated in Fig. 1.

## II. CHARACTERIZATION OF THE CAVITY

For a single port cavity, the reflection coefficient  $S_{11}$  is given by,

$$|S_{11}|(\omega) = \left| 1 - \frac{\kappa_e}{-i(\omega - \omega_c) + (\kappa_i + \kappa_e)/2} \right| \quad (1)$$

where  $\kappa_e$  is the external coupling rate,  $\kappa_i$  is the internal dissipation rate, and  $\omega_c$  is the cavity resonance frequency. Fig. 2(a) shows the measurement of  $S_{11}$  at  $T = 14$  mK. The gray

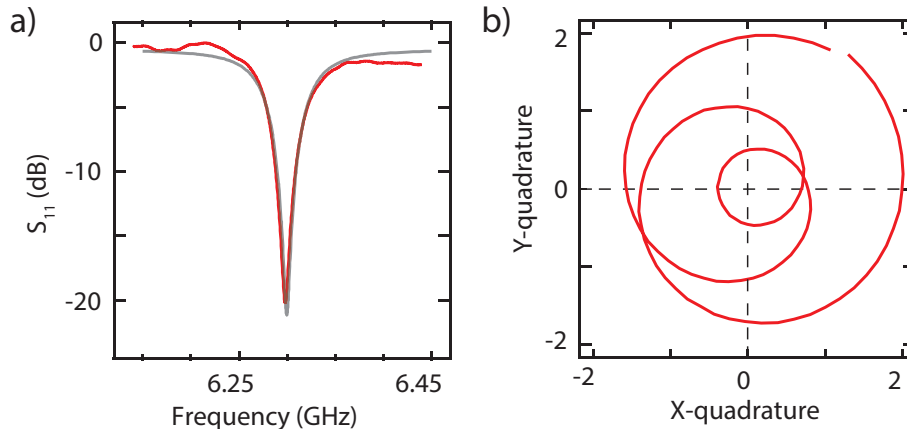


FIG. 2: (a) Measurement of the normalized reflection coefficient  $S_{11}$  of the cavity at base temperature (red curve). The gray curve is the fit to the data yielding an internal dissipation rate  $\kappa_i = 2\pi \times 25.8$  MHz and an external coupling rate  $\kappa_e = 2\pi \times 31.0$  MHz. (b) Two quadratures of  $S_{11}$  (raw data) plotted against each other, reflecting the over-coupled behavior of the cavity.

curve in Fig. 2(a) is the numerically fitted curve using equation 1. To differentiate between over-coupling ( $\kappa_e > \kappa_i$ ) and under-coupling ( $\kappa_i > \kappa_e$ ) limits, one must measure the phase  $\arg(S_{11}(\omega))$  of the reflection coefficient. Equivalently, one can also parametrically plot two quadratures  $X = \text{Re}(S_{11})$  and  $Y = \text{Im}(S_{11})$  against each other. For an overcoupled cavity the resonance circle appears to enclose the origin as shown in Fig 2(b). The additional circle (larger diameter) is due to the phase wrapping due the finite electrical length between the device and the circulator.

### III. HOMODYNE DETECTION SCHEME

To detect the mechanical motion, we use the superconducting microwave cavity in a homodyne detection setup. The mechanical resonator is actuated by capacitive forces by adding a radio-frequency signal  $V_{AC}$  (near the mechanical resonance frequency) and a DC voltage  $V_{DC}$  to the feedline (using a bias-tee at low temperature). Due to electrostatic force, the mechanical resonator experiences a modulating force of magnitude given by  $\frac{dC_c}{dx} V_{DC} V_{AC}$ , where  $C_c$  is the capacitance between the mechanical resonator and the feedline electrode.

To detect the mechanical motion, we use the cavity as an interferometer. The cavity is driven by a signal at its resonance frequency  $\omega_c$  acting as the carrier signal. The motion of

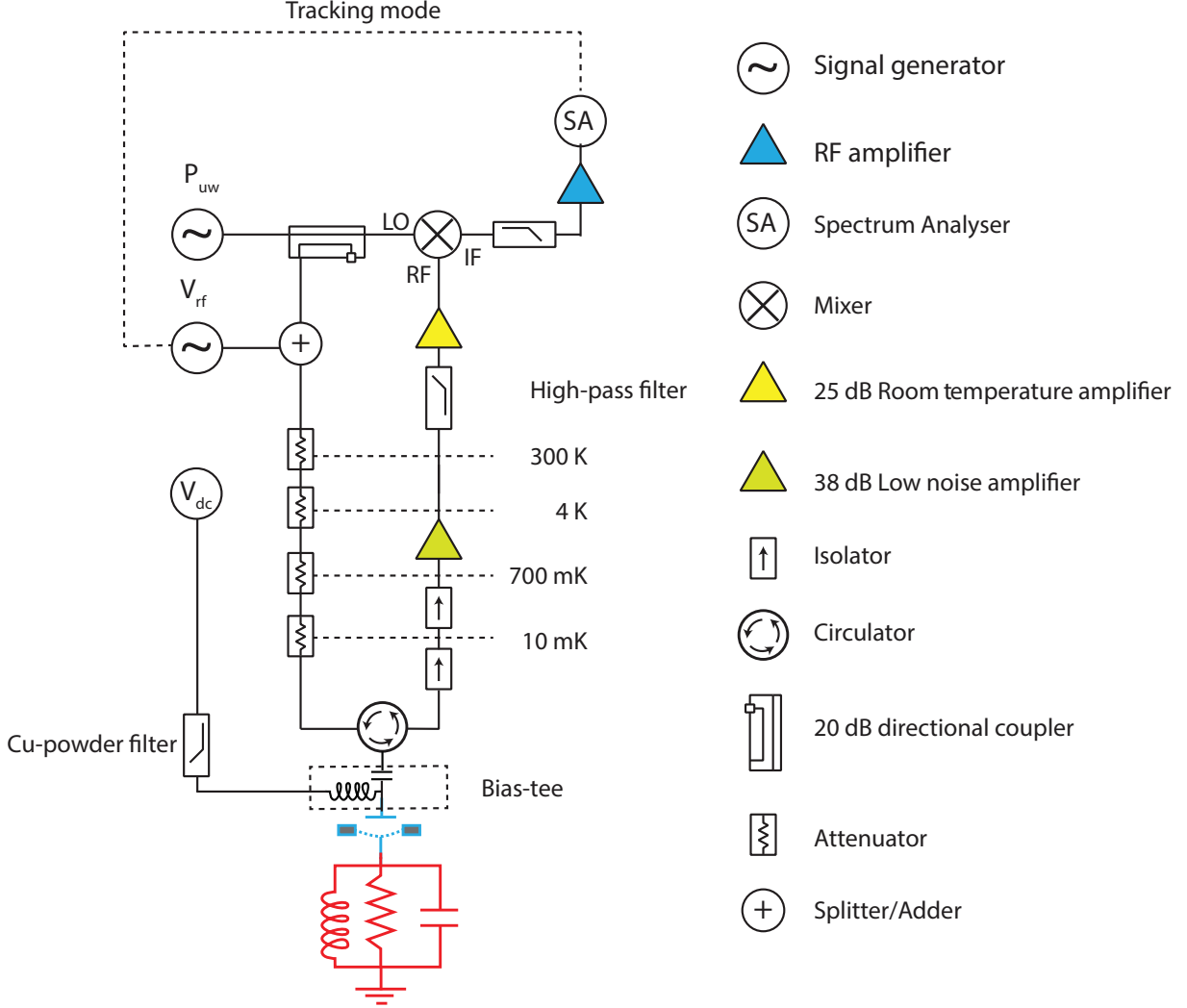


FIG. 3: Schematic diagram of the homodyne detection setup.

the mechanical resonator (at frequency  $\omega_m$ ) modulates this signal and produces mechanical sidebands at frequencies  $\omega_c \pm \omega_m$ . The sideband signal along with the carrier is amplified by a low noise amplifier and then passed through a high-pass filter (3 GHz-9 GHz) before entering the second amplifier at room temperature. The amplified signal is then mixed down to RF frequencies by using a mixer (MiniCircuits-ZMX8GH+). To avoid any phase drifts, we have used the same source to drive the local oscillator (LO) port of the mixer. The mixed-down RF signal is filtered and amplified further before entering the spectrum analyzer. The spectrum analyzer is used in tracking mode with the signal generator used to mechanically drive the resonator, thus allowing to record the response as function of actuation frequency. A complete schematic of the measurement scheme is shown in Fig 3.



#### IV. FITTING THE ASYMMETRIC RESPONSE WITH FANO-FUNCTION

Due to finite isolation of the circulator for low frequency RF signals (used for mechanical driving), part of the RF signal leaks directly into the output measurement chain, producing frequency independent constant background signal in the measurement. This background signal interferes with the signal generated due to the mechanical motion of the resonator, giving a Fano-lineshape in the measured data. Taking this background signal into account, the measured response can be fitted to the following Fano-form, also known as skewed-Lorentzian

$$\tilde{V}_{measured} = \frac{V_0}{1 - 2iQ_m \frac{f-f_m}{f_m}} + \alpha e^{i\phi} \quad (2)$$

where  $f_m$  is the mechanical resonant frequency,  $Q_m$  is the mechanical quality-factor,  $\alpha e^{i\phi}$  is a small background signal with amplitude  $\alpha$  and phase  $\phi$ .

#### V. MODEL FOR THE ESTIMATION OF THE MECHANICAL AMPLITUDE

The combined effect of charging the transmission line and applying an AC-voltage leads to a force on the drum given by:

$$F = \frac{1}{2} \frac{\partial C}{\partial x} V^2 = \frac{1}{2} \frac{\partial C}{\partial x} (V_{DC} + V_{AC})^2 = \frac{1}{2} \frac{\partial C}{\partial x} (V_{DC}^2 + 2V_{DC}V_{AC} + V_{AC}^2) \quad (3)$$

The first term  $V_{DC}^2$  is a constant force which will attract the drum, increasing the stress of its membrane and thus lowering its frequency quadratically. The last term  $V_{AC}^2$  can be neglected. We will call the second term the AC driving force  $F_{AC}$ . By assuming the capacitance of the drum to the transmission line to be that of a vacuum-gap, parallel plate capacitor, we can write:

$$F_{AC} = V_{AC}V_{DC} \frac{\partial}{\partial x} \left( \frac{\epsilon_0 A}{\bar{d} + x} \right) \quad (4)$$

Where  $\epsilon_0$  is the permittivity of vacuum,  $A$  is the area of the capacitive plates,  $\bar{d}$  is the gap between the plates after having taken into account the constant displacement induced by the gate voltage.  $x$  is the vertical displacement from this equilibrium position and is taken as a small quantity  $x \ll \bar{d}$  resulting in the expression for the AC drive:

$$F_{AC} = -V_{AC}V_{DC} \left( \frac{\epsilon_0 A}{\bar{d}^2} \right) \quad (5)$$

Assuming the drum behaves as a damped harmonic oscillator with an effective mass  $m$ , eigen frequency  $\omega_m$  and quality factor  $Q_m$ , the amplitude of the mechanical oscillations can be related to the strength of the (resonant) drive:

$$x_0 = \frac{F_{AC}Q_m}{m\omega_m^2} \quad (6)$$

In this analysis the effective mass is taken to be the total mass of the drum (this choice defines the amplitude  $x_0$  which is otherwise ambiguous due to the geometry of the drum). We calculate the amplitude of the AC-voltage from the input power at the device  $P_{DUT}$

$$V_{AC} = \sqrt{2Z_0P_{DUT}} \quad (7)$$

where  $Z_0 = 50 \Omega$  is the characteristic impedance of our line. This power can be calculated from the output power of our signal generator and an estimation of the attenuation on the input measurement chain. The following steps are then taken:

- We convert the input power at our signal generator to the force acting upon the drum using 7 and 5
- We associate the peak measured power  $p_0$  with the amplitude mechanical oscillation  $x_0$  using 6
- We convert the power received off-resonance  $p$  to a mechanical amplitude  $x = x_0\sqrt{p/p_0}$

Alternatively, one could also use the measured homodyne signal to work out the amplitude of the mechanical resonator under a coherent drive. For a single port cavity driven at its resonant frequency ( $\Delta = 0$ ), amplitude of the drumhead resonator can be written as,  $x_p^2 = \frac{\omega_m^2 + \kappa^2/4}{(\eta G)^2} \frac{P_o}{P_i}$ , where  $G$  is the cavity pull-in parameter,  $\eta = \kappa_e/\kappa$  is the coupling fraction,  $P_o$  is the homodyne power (after removing gain, loss of the output chain, and conversion loss of the mixer), and  $P_i$  is the injected power outside the cavity.

## VI. ADDITIONAL DATA FROM SECOND DEVICE

Additional data from second device showing the nonlinear damping of the mechanical resonator is shown in Fig. 4.

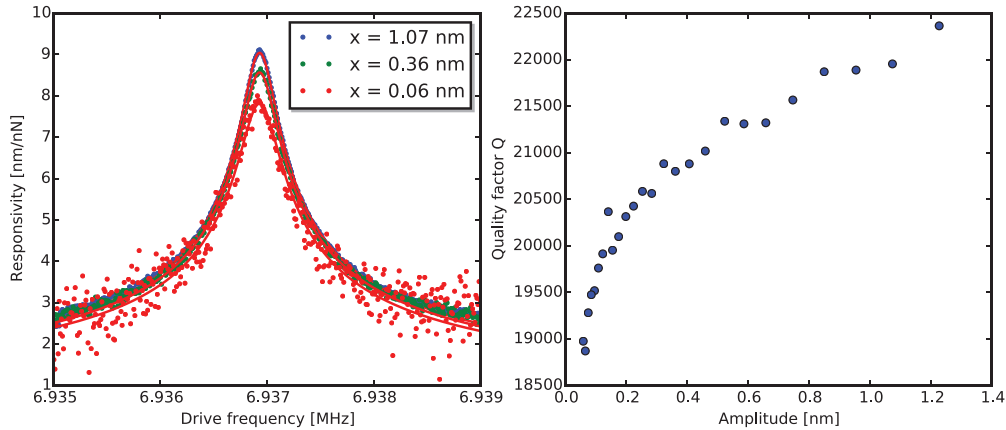


FIG. 4: Mechanical response and mechanical quality factor as a function of power

## VII. ESTIMATION OF THE GAP BETWEEN THE DRUM AND THE BOTTOM ELECTRODE

The gap between the drum and the bottom electrode can be estimated from the total inductance of the high impedance resonator. The total inductance of the microstrip resonator is estimated to be 3.43 nH using finite element modeling and considering kinetic inductance of Mo-Re. Total capacitance is calculated from geometric inductance and the cavity frequency. Coupling quality factor in single port cavity is given as,

$$Q_{ext} = \frac{C_l + C_c}{\omega_c C_c^2 Z_0} \quad (8)$$

where  $C_c$  is coupling capacitance,  $\omega_c$  is resonance frequency of the cavity,  $Z_0$  is input impedance of transmission line, and  $C_l$  is lumped capacitance of the resonator line. From the parameters of cavity characterization, coupling capacitance is 21.5 fF. Assuming a parallel plate capacitor model, we found the mean position of the drum head resonator  $\bar{d}$  to be 291 nm for the device represented in Fig. 4 of main text.

Alternatively, one can perform opto-mechanically induced absorption (OMIA)<sup>1</sup> leading to a measurement of the cooperativity  $C = 4g^2/\kappa\Gamma$  where  $\kappa$  is the cavity line-width,  $\Gamma$  the mechanical line-width and  $g = G\sqrt{n_d}\sqrt{\hbar/2m\omega_m}$  is the opto-mechanical coupling strength where the average number of photons in the cavity  $n_d$  in that particular measurement is calculated from our estimation of the input attenuation. OMIA thus provides a measure

TABLE I: Important parameters of the devices

Parameters	Device 1	Device 2
Density of MoRe	14.5 g/cm <sup>3</sup>	14.5 g/cm <sup>3</sup>
Diameter of drum	30 μm	30 μm
Gap between the drumhead and the feedline	291 nm	481 nm
Thickness of the mechanical resonator	125 nm	131 nm
Equivalent lumped inductance of the cavity	3.43 nH	2.37 nH
Drumhead capacitance	21.5 fF	12.6 fF
Cavity pull-in parameter $\frac{G}{2\pi}$	$1.2 \times 10^{15}$ Hz/m	$8.53 \times 10^{14}$ Hz/m
Total attenuation on low frequency drive line	65 dB	55 dB

of the cavity pull-in parameter  $G = d\omega_c/dx = 8.53 \times 10^{14}$  Hz/m. For a  $\lambda/4$  resonator, the pull-in parameter assuming a parallel plate capacitor is given by:

$$G = \frac{2Z_0\omega_r^2 \epsilon A}{\pi \bar{d}^2} \quad (9)$$

from this we estimate the mean position of the drum head resonator  $\bar{d}$  to 481 nm for the device represented in Fig. 4 of the supplementary materials.

**VIII. PARAMETERS FOR THE DEVICES SHOWN IN THE MAIN TEXT (DEVICE 1) AND IN SUPPLEMENTAL MATERIALS (DEVICE 2)**

---

<sup>1</sup> Singh, V., Bosman, S. J., Schneider, B. H., Blanter, Y. M., Castellanos-Gomez, A., and Steele, G. A *Nature Nanotechnology* **9**(10), 820-824 August (2014).